Chemosphere 294 (2022) 133441

Contents lists available at ScienceDirect

Chemosphere

journal homepage: www.elsevier.com/locate/chemosphere

Hollow porous cobalt oxide nanobox as an enhanced for activating monopersulfate to degrade 2-hydroxybenzoic acid in water

Duong Dinh Tuan [a,1], Cong Khiem [a,1], Eilhann Kwon [b], Yiu Fai Tsang [c,d], Sanya Sirivithayapakorn [e], Bui Xuan Thanh [f], Grzegorz Lisak [g,h], Hongta Yang [i,**], Kun-Yi Andrew Lin [a,*]

[a] Department of Environmental Engineering & Innovation and Development Center of Sustainable Agriculture, National Chung Hsing University, 145 Xingda Rd, South Dist, Taichung City, 402, Taiwan
[b] Department of Environment and Energy, Sejong University, 209 Neungdong-ro, Gunja-dong, Gwangjin-gu, Seoul, Republic of Korea
[c] Department of Sc Environmental Engineering Department, Faculty of Engineering, Kasetsart University, Bangkok, Thailand Vironmental Studies, Thailand
[d] The Education University of Hong Kong, Tai Po, New Territories, 999077, Hong Kong
[e] Environmental Engineering Department, Faculty of Engineering, Kasetsart University, Bangkok, Thailand
[f] Key Laboratory of Advanced Waste Treatment Technology & Faculty of Environment and Natural Resources, Ho Chi Minh City University of Technology (HCMUT), Vietnam National University Ho Chi Minh (VNU-HCM), 268 Ly Thuong Kiet Street, District 10, Ho Chi Minh City, 700000, Viet Nam
[g] School of Civil and Environmental Engineering, Nanyang Technological University, 50 Nanyang Avenue, 639798, Singapore
[h] Residues and Resource Reclamation Centre (R3C), Nanyang Environment and Water Research Institute, Nanyang Technological University, 1 Cleantech Loop, Clean Tech One, 637141, Singapore
[i] Department of Chemical Engineering, National Chung Hsing University, 250 Kuo- Kuang Road, Taichung, Taiwan

HIGHLIGHTS

- Hollow porous Co_3O_4 nanobox (PCNB) is derived from etched cubic Co-MOF.
- PCNB shows more superior surficial properties than commercial Co_3O_4 NP.
- PCNB surpassingly outperforms the benchmark Co_3O_4 NP for degrading HBA.
- PCNB can be reused to effectively activate MPS for degrading HBA completely.
- DFT calculation is performed to elucidate degradation process of HBA by PCNB.

GRAPHICAL ABSTRACT

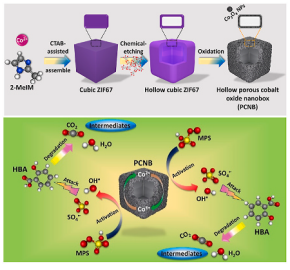

ARTICLE INFO

Handling Editor: Jun Huang

Keywords:
Pharmaceutical and personal care products
2-Hydroxybenzoic acid
Monopersulfate

ABSTRACT

As 2-hydroxybenzoic acid (HBA) represents a typical pharmaceutical and personal care product (PPCP), constant releasing of HBA into the environment poses threats to the ecology, and thus it is critical to develop effective techniques to remove HBA from water. Recently, sulfate radical ($SO_4^{\bullet-}$)-based advanced oxidation processes involved with monopersulfate (MPS) activation are proven as effective approaches for eliminating PPCPs from water, and Co_3O_4 is recognized as a capable catalyst for activating MPS. Therefore, great interests have arisen to develop Co_3O_4-based catalysts with advantageous morphologies and characteristics for enhancing catalytic

* Corresponding author.
** Corresponding author.
E-mail addresses: hyang@nchu.edu.tw (H. Yang), linky@nchu.edu.tw (K.-Y.A. Lin).
[1] These authors contribute to this study equally.

https://doi.org/10.1016/j.chemosphere.2021.133441
Received 28 October 2021; Received in revised form 13 December 2021; Accepted 23 December 2021
Available online 28 December 2021

Hollow
Co_3O_4

activities. Therefore, a special Co_3O_4-based material is proposed in this work. Through a surfactant-assisted strategy, a cubic Co-MOF is prepared and used as a precursor, which is etched to afford hollow structure, and then transformed into hollow porous Co_3O_4 nanobox (PCNB). PCNB can exhibit distinct reactive surface with abundant surface oxygen vacancy as well as physical properties in comparison to the commercial Co_3O_4 NPs (com-Co_3O_4 NP), thereby leading to the outstanding catalytic activity of PCNB for activating MPS to degrade HBA. The activation energy (E_a) of 46.2 kJ/mol is also calculated using PCNB + MPS system, which is much lower than most of recent reported studies for activating MPS. PCNB could be also reusable over 5 consecutive HBA degradation cycles. The activation mechanism of MPS by PCNB and HBA degradation pathway are also comprehensively elucidated via experimental evidences and the theoretical calculation to offer insightful information of development of Co_3O_4 for HBA degradation.

1. Introduction

Pharmaceutical and personal care products (PPCPs) released into water may potentially harm ecological system as well as human life due to their potential carcinogenic effect and toxicity (Ebele et al., 2017). Among various PPCPs, 2-hydroxybenzoic acid (HBA) represents one of the most common PPCPs, which is widely-used in the production of food preservatives, medical and cosmetic products (Boullard et al; Savun--Hekimoglu and Ince, 2017). As HBA is consistently released into the environment via different pathways, and various HBA concentrations have been ubiquitously detected in water systems (Lapworth et al., 2018; Hu et al., 2016), causing negative impact on human health and living organisms, it is critical to develop techniques to remove HBA from wastewater. For example, a high concentration of HBA (i.e., 1225 ng/L) was detected in ground water (Lapworth et al., 2018) while HBA was also found in tap water with its concentration ranged from 16.6 ng/L to 41.2 ng/L (Hu et al., 2016). In wastewater treatment plans, the residue concentration of HBA was also determined as 30 ng/L (Carmona et al., 2014).

While various treatment techniques including adsorption (Otero et al., 2004), filtration (Karnik et al., 2007), biological (Wang et al., 2017a), electrochemical (Guinea et al., 2008) and photocatalytic treatments (Wu et al., 2019) have been attempted to eliminate HBA from water, these techniques still suffer from relatively low removal capabilities (Wang et al., 2021). Recently, sulfate radical-based advanced oxidation processes ($SO_4^{\bullet-}$-AOPs) associated with monopersulfate (MPS) activation has been considered an effective approach for eliminating organic pollutants owing to several merits of $SO_4^{\bullet-}$ such as broad pH stability, high redox potentials, and long life-span (Guerra-Rodríguez et al., 2018). For instance, our group has developed a Co-embedded in N-doped carbon nanocapsule for MPS activation to effectively degrade HBA in water (Tuan et al., 2021a). Another research work by Tuan et al. also prepared a porous nanoplate Co_3O_4-based $SO_4^{\bullet-}$-AOPs to eliminate HBA (Tuan et al., 2020a).

To effectively acquire $SO_4^{\bullet-}$, heterogeneous catalysts have been increasingly employed, and Cobalt (Co)-based catalysts have shown outstanding catalytic activities for MPS activation (Hu and Long, 2016). For instance, Liu et al. prepared a N-doped porous Co@C nanaboxes derived from ZIF-67 for persulfate activation to effectively remove *p*-chloroaniline (Liu et al., 2019). Another research work by Liu's group further employed a MOF-based material as a template to synthesize a metal-free N-doped porous carbon for activating peroxydisulfate (Liu et al., 2020). In addition to Co-based materials, a Cu-MOF derived into Cu nanoparticles decorated in a three-dimensional reduced graphene oxide (3D RGO) network was also utilized for peroxydisulfate activation (Liu et al., 2021). Additionally, cobalt oxide (Co_3O_4) has been validated to efficiently activate MPS to degrade refractory organic contaminants (Xu et al., 2020; Deng et al., 2017). However, since the catalytic activation of MPS is conducted in aqueous media, Co_3O_4 particles, especially nanoparticles (NPs), are usually aggregated, thus diminishing their catalytic activities (Deng et al., 2017). Therefore, great interests have arisen to develop Co_3O_4-based catalysts with advantageous morphologies and characteristics for enhancing catalytic activities.

Therefore, in this work, we propose to fabricate a special Co_3O_4-based material derived from a cobaltic metal organic framework (Co-MOF). Through a surfactant-assisted strategy, Co-MOF with a cubic morphology was first prepared and employed as a precursor, which is then modified via chemical-etching process with tannic acid (TAN) to afford hollow structure, and subsequently transformed into hollow porous Co_3O_4 nanobox (PCNB) via calcination. The as-fabricated PCNB is expected to exhibit the unique morphology and distinct surficial properties from the commercial Co_3O_4 NPs (com-Co_3O_4 NP). The effects of various parameters such as catalyst and MPS dosages, temperatures, pH, co-existing compounds were examined to explore how this PCNB would behave differently from com-Co_3O_4 for further elucidating the structure-property-activity relationship. Moreover, radical species from PCNB-activated MPS system for degrading HBA are also determined via quenching experiment and electron spin resonance (ESR). The degradation pathway of HBA is also elucidated based on the detected intermediates, and density functional theory (DFT) calculation. By experimental and theoretical investigations, insightful behaviors and mechanisms of HBA degradation by nanostructured Co_3O_4+MPS system are further elucidated.

2. Experimental

In general, Co-MOF with the cubic morphology would be fabricated and employed as a precursor, which was then etched by tannic acid (TAN) to convert the cubic Co-MOF into a hollow structure as illustrated in Fig. 1(a). This resulting hollow cubic Co-MOF would be then calcined to generate hollow porous Co_3O_4 nanobox (PCNB). The comprehensive preparation protocols, material characterizations and batch-type tests of HBA degradation are given in the supporting information (SI). Com-Co_3O_4 NP was purchased from Alfa Aesar (its size range of 50–80 nm, and purity of 99%) as a reference material for comparison with PCNB.

3. Results and discussion

3.1. Characterizations of PCNB

The formation of the as-prepared materials was first characterized. Fig. 1(b) shows the XRD patterns of the pristine cubic Co-MOF, in which several noticeable diffraction peaks corresponding to the reported Co-MOF were observed, verifying the successful formation of Co-MOF (Andrew Lin and Chen, 2016; Tuan and Lin, 2018). After chemical-etching with TAN and then calcined in air, the resultant material exhibited distinct XRD patterns as displayed in Fig. 1(c). Particularly, various notable diffraction peaks at 19°, 31.4°, 36.8°, 38.6°, 44.8°, 55.5°, 59.3°, 65.1°, 74.1° and 77.3° could be ascribed to the planes of (111), (220), (311), (220), (400), (422), (511), (440), (620), and (533) of Co_3O_4 (JCPDS #42–1467), respectively. This result validated the complete transformation from pristine cubic Co-MOF into Co_3O_4.

Besides, the appearances of these as-prepared materials were further visualized. Fig. 2(a) and (b) present SEM and TEM images of the pristine Co-MOF, showing that the cubic Co-MOF with smooth surfaces had been successfully synthesized, and the size of these cubic Co-MOF was up to 500–800 nm. When this cubic Co-MOF was etched by TAN, the resulting product still retained the cubic morphology (Fig. S1(a)). However, the

internal content of this product was removed, while the external layer (size of *ca.* 50–60 nm) was remained (as displayed in Fig. S1(b)), leaving a huge void inside the cubic Co-MOF.

Moreover, once this hollow product was further calcined, the resultant product exhibited a box-like appearance with the presence of many pores after calcination process (Fig. 2(c)). The TEM of this box-like product in Fig. 2(d) reveals that the hollow structure was still preserved. A closer view in Fig. 2(e) further verifies that this product was also comprised of many small NPs which were distributed evenly throughout the entire substrate. The size of these NPs measured as shown in the inset of Fig. 2(e), showing that these NPs were very fine with diameters of 8–12 nm. The lattice-resolved HRTEM of this material in Fig. 2(g) presents two specific *d*-spacing values of 0.241 nm and 0.285 nm, which can be attributed to (311) and (220) planes of Co_3O_4, respectively, indicating that the aforementioned NPs were Co_3O_4. This also validates that the hollow cubic Co-MOF had been completely converted into hollow porous Co_3O_4 nanobox (PCNB). The inset in Fig. 3(g) provides the selected area electron diffraction (SAED) pattern of PCNB, further demonstrating that PCNB had a polycrystalline structure (Tuan et al., 2020b; Tsai et al., 2020). Besides, the elemental composition of PCNB was analyzed as illustrated in Fig. S2(a), in which only Co and O signals were obtained, further confirming the formation of Co_3O_4 in PCNB. The elemental mapping of PCNB further reveals the uniform distribution of Co and O over the nanobox surface as shown in Fig. S2 (c)–(d).

In addition, IR spectra of the pristine cubic Co-MOF and the as-prepared PCNB were also characterized to verify the functional groups of these two materials as presented in Fig. 3(a). In the case of Co-MOF, several noticeable absorption peaks in a range from 500 to 1500 cm^{-1} could be assigned to imidazole ring (Lin and Chang, 2015). On the other hand, the as-prepared PCNB exhibited totally different absorption peaks. Specifically, two intense absorption peaks at 565 and 660 cm^{-1} could be ascribed to the stretching vibrations of cobalt oxide for tetrahedrally-coordinated Co^{2+} ions and octahedrally-coordinated Co^{3+} ions (Herrero et al., 2007), respectively. The other absorption peaks at 1630 cm^{-1} and 3410 cm^{-1} could be attributed the O–H stretching and bending vibration modes, possibly resulted from water molecules adsorbed on PCNB surface (Hu et al., 2015).

Besides, Raman spectroscopies of PCNB and the com-Co_3O_4 NP were further examined. Both materials exhibited similar peaks (Fig. 3(b)), which corresponded to Raman active vibration modes (i.e., $A_{1g} + E_g + 3F_{2g}$) of Co_3O_4 (Tang et al., 2008), further indicating the high-crystalline formation of Co_3O_4 in PCNB after calcination. Nonetheless, as revealed in Fig. 3(c) and (d), the peaks of PCNB at $F_{2g}^{(1)}$ and A_{1g} regions were shifted in comparison with that of com-Co_3O_4 NP. Particularly, the peak at $F_{2g}^{(1)}$ in PCNB was shifted from 190 cm^{-1} to 192 cm^{-1} while the peak at A_{1g} was shifted from 677 cm^{-1} to 680 cm^{-1}. Since $F_{2g}^{(1)}$ was ascribed to the mobility of oxygen atoms in the octahedrally coordinated Co^{3+}-O^{2-} (CoO_6) and A_{1g} was assigned to the tetrahedrally coordinated Co^{2+}-O^{2-} (CoO_4) in Co_3O_4 (Tang et al., 2008; Farhadi et al., 2016), these shifting suggested that PCNB possessed abundant oxygen vacancies on the surface than that of com-Co_3O_4 NP (Wang et al., 2016), which could probably contribute to their distinct catalytic activities for MPS activation.

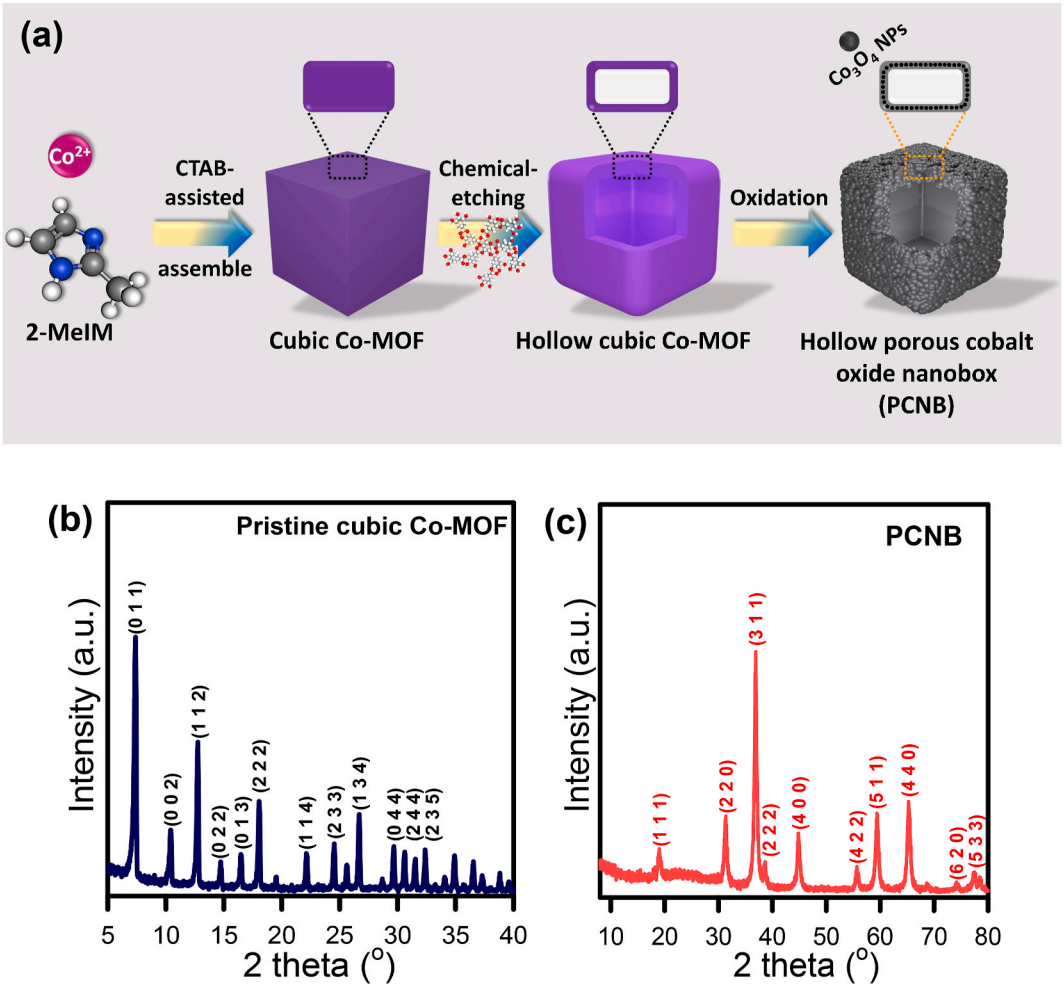

Fig. 1. (a) Schematic illustration for PCNB preparation; XRD analysis of (b) pristine cubic Co-MOF, and (c) the calcined product (PCNB).

Additionally, the surface chemistry of PCNB was further characterized by XPS to determine the element states in PCNB. Fig. 4(a) shows a full-scan survey spectrum, in which Co and O signals were mainly observed, which was well-matched with EDS analysis. The Co2p core-level spectra of PCNB in Fig. 4(b) were further examined, in which multiple underlying peaks were deconvoluted. Specifically, two peaks at 779.6 and 794.6 eV could be ascribed to Co^{3+} while two peaks at 781.4 and 796.7 eV could be assigned to Co^{2+}, further verifying the formation of Co_3O_4 in PCNB (Zhang et al., 2018). On the other hand, O1s spectra of PCNB were also determined as shown in Fig. 4(c), in which two noticeable underlying peaks could be observed at 529.6 and 531.1 eV, corresponding to lattice oxygen (O_{latt}) and chemisorbed oxygen species (O_{ads}) (Tuan et al., 2021b).

On the other hand, as the reducibility of metal oxide represents another crucial feature in oxidation reactions, H_2-TPR analysis was then employed to determine the reductive behavior of PCNB and com-Co_3O_4 NP. H_2-TPR profiles in Fig. 4(d) reveal that com-Co_3O_4 NP showed two reduction peaks while PCNB exhibited three reduction peaks.

Since cobalt oxide commonly showed a two-stage reduction process (i.e., the first stage is the reduction of Co^{3+} to Co^{2+}, and the second stage is the reduction of Co^{2+} to metallic Co (Co^0)) (de Rivas et al., 2011), com-Co_3O_4 NP exhibited two reduction peaks, in which the first peak centered at 466 °C could be ascribed to the first reduction stage, and the other peak centered at 503 °C could be ascribed to the second reduction stage. However, in case of PCNB, the H_2-TPR profile of PCNB presented three reduction peaks. In particular, the first peak centered at 304 °C could be assigned to the reduction stage where Co^{3+} reduced to Co^{2+} whereas the second peak centered at 349 °C and the third peak centered at 397 °C could be ascribed to the second reduction stage, in which Co^{2+} reduced to metallic Co in cluster forms and bulk forms (Silva et al., 2020), respectively. More interestingly, the reduction peaks in PCNB were much less overlapped compared with that of com-Co_3O_4 NP with the reduction temperatures appeared in PCNB were obviously lower. This result indicated that PCNB possessed more reactive surface than that of com-Co_3O_4 NP (Fuchigami et al., 2018), contributing to their distinct catalytic activities in the catalytic oxidation reactions (Gong and Zeng, 2021).

Furthermore, the physical characteristics of PCNB were also necessarily studied using N_2 adsorption-desorption isotherms. As depicted in Fig. 4(e), PCNB exhibited N_2 adsorption-desorption isotherms of IUPAC type III and IV isotherms, implying the presence of pores in PCNB. The inset in Fig. 4(e) illustrates that PCNB possessed mesopores and macropores. The BET surface area of PCNB was then determined as 66.61 cm^2/g with a pore volume of 0.39 cm^3/g. As com-Co_3O_4 NP was also used to activate MPS, which also possessed different reductive behavior in comparison with PCNB, it was also necessary to examine the textural properties of com-Co_3O_4 NP. Fig. S3(b) illustrated the N_2 sorption isotherms of com-Co_3O_4 NP, and the BET surface area of com-Co_3O_4 NP was calculated as 2.8 m^2/g with a pore volume of 0.002 cm^3/g, which are much lower than that of PCNB, possibly due to the agglomeration of these Co_3O_4 NPs (Fig. S3(a)).

Moreover, since the degradation of HBA was conducted in the aqueous batch-type experiments, it was crucial to examine the charges of PCNB surface at various pH values. The zeta potentials profiles of PCNB displayed in Fig. 4(f) demonstrated that the surface charge of PCNB was positive in acidic and neutral conditions, which became negatively in alkaline conditions. Particularly, at pH = 3, PCNB exhibited a surface charge of +18.54 mV, which was slightly decreased to +9.8 mV when pH was adjusted to 5. Once pH = 7, the surface charge of PCNB was only +3.12 mV, which was further declined to −7.6 mV and −14.4 mV at pH = 9 and 11, respectively.

3.2. Catalytic degradation of HBA by PCNB activated MPS

Before evaluating the degradation efficiency of HBA using PCNB activated MPS, it would be crucial to verify whether HBA can be

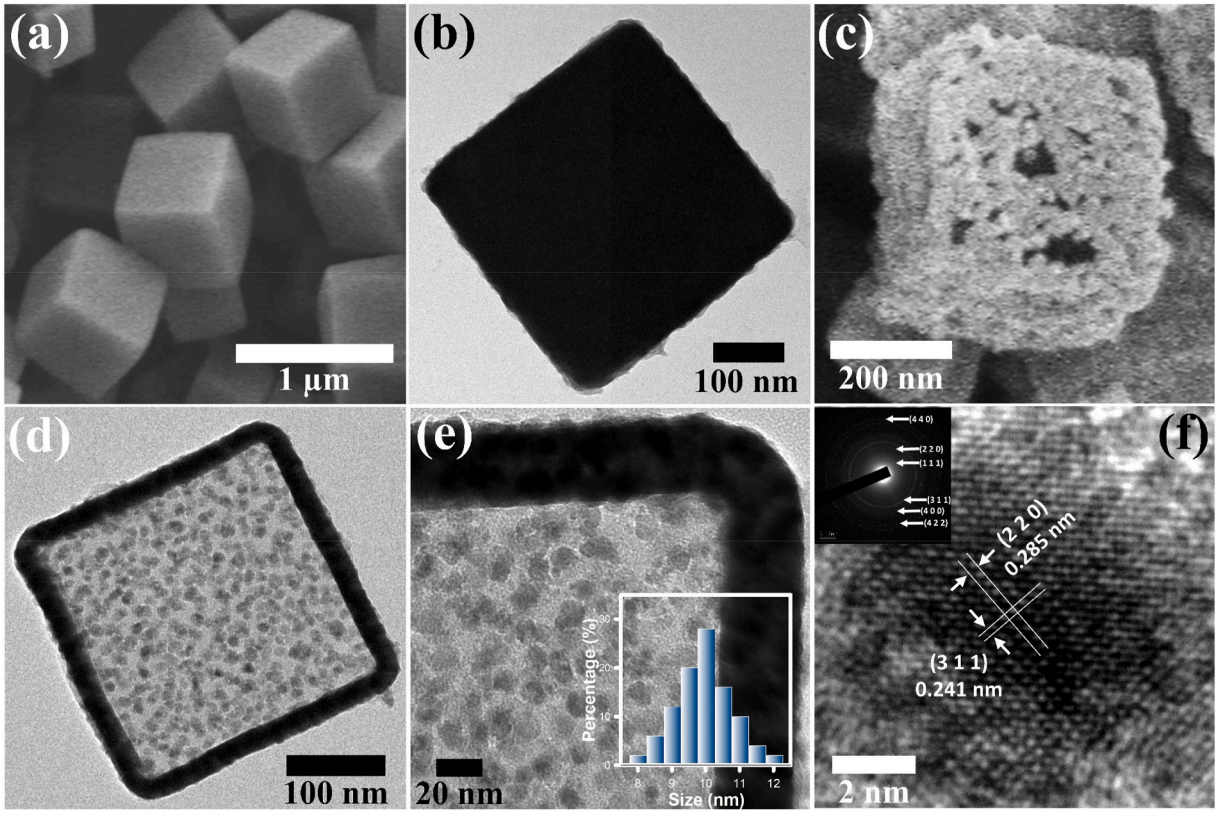

Fig. 2. (a) SEM and (b) TEM images of pristine cubic Co-MOF; (c) SEM and (d) TEM images of PCNB; and (f), (g) HRTEM images of PCNB (the inset is the SAED of PCNB).

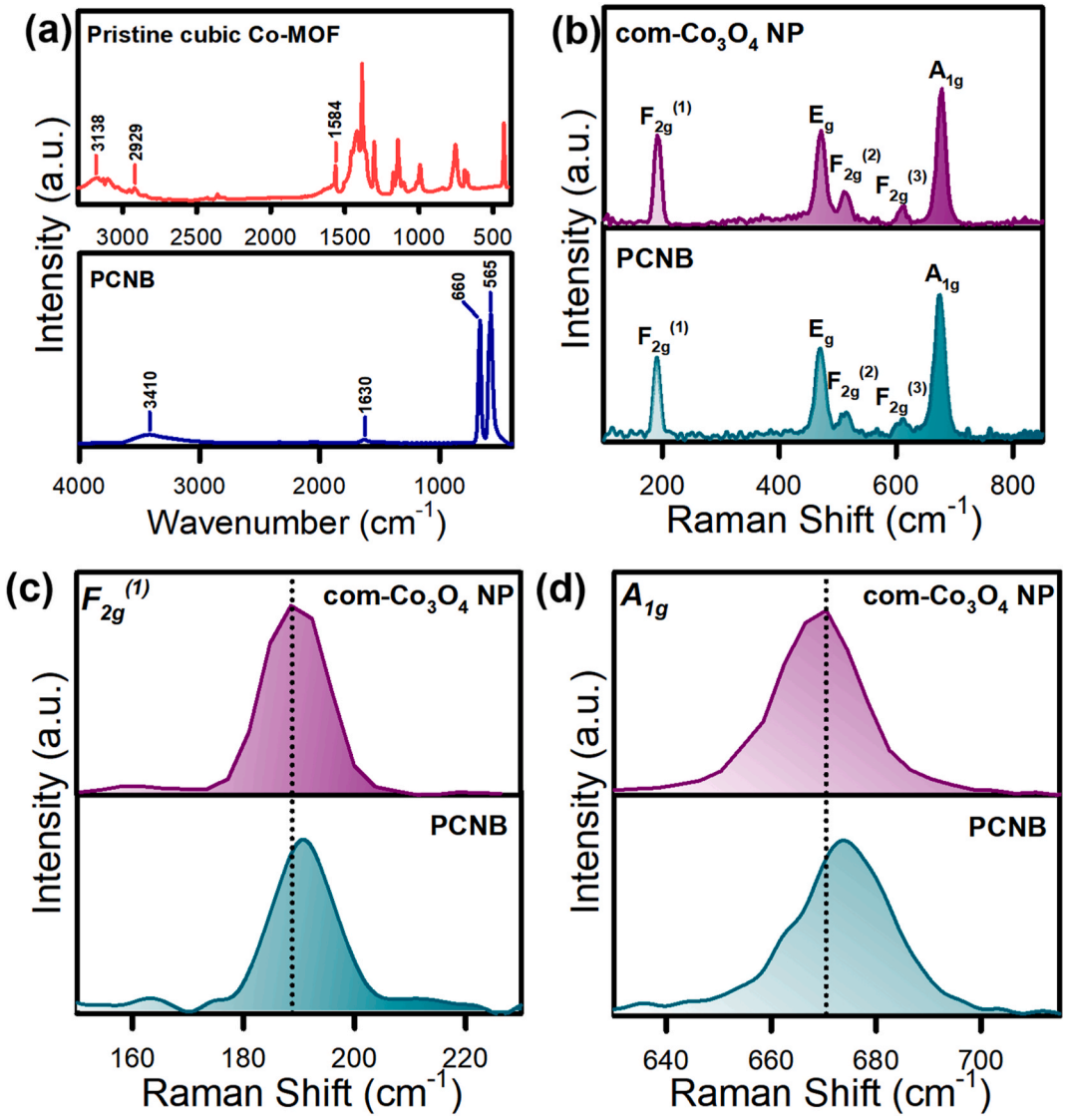

Fig. 3. (a) IR spectra of com-Co_3O_4 and PCNB; (b) Raman spectroscopies of com-Co_3O_4 NP and PCNB, (c) and (d) short-range Raman spectrum at $F_{2g}^{(1)}$ and A_{1g}.

removed via adsorption. As shown in Fig. 5(a), the concentration of HBA remained almost the same after 30 min when PCNB was individually used, suggesting that HBA was negligibly removed via adsorption. Besides, it can be noticed that HBA degradation efficiency was also ineffective in the presence of MPS only as C_t/C_0 merely reached to 0.93, implying that the self-activation of MPS could not efficiently degrade HBA as the generation of reactive oxygen species (ROS) without activation was critically slow. When the pristine cubic Co-MOF was used to activate MPS, the degradation efficiency of HBA was also insignificantly improved as C_t/C_0 was 0.88, suggesting that pristine cubic Co-MOF was also ineffective for activating MPS. However, once PCNB was employed to activate MPS, the concentration of HBA was significantly reduced and completely degraded within 30 min, indicating that MPS was certainly activated to quickly generate ROS in the presence of PCNB. Since HBA could be effectively degraded using PCNB + MPS system, the total organic carbon (TOC) was necessarily measured. As depicted in Fig. S4, ca. 69% of TOC for HBA could be afforded in 60 min, indicating that HBA was certainly decomposed by PCNB + MPS system. This information had been added in the main text. Please see the revised manuscript.

For comparison, as PCNB was comprised of Co_3O_4 NPs, the commercial Co_3O_4 NP (com-Co_3O_4 NP) was then employed to activate MPS for HBA degradation. As depicted in Fig. 5(a), *ca.* 35% of HBA concentration was moderately degraded in 60 min, revealing that com-Co_3O_4 NP could also activate MPS to degrade HBA. However, the HBA degradation efficiency of com-Co_3O_4 NP + MPS was still much lower in comparison with that of PCNB + MPS. As discussed in the earlier section, PCNB possessed outstanding physicochemical properties (i.e., higher degree of abundant oxygen vacancies on the surface and more reactive surface in comparison with com-Co_3O_4 NP. Moreover, the specific surface area of PCNB was also much higher than that of com-Co_3O_4 NP, possibly due to the serious agglomeration of com-Co_3O_4 NP (Fig. S3(a)), thus hindering the active cites and resulting in ineffective degradation efficiency. These distinct properties between these two materials contributed to their different catalytic activities for MPS activation. This result further confirmed that PCNB could be a promising heterogeneous catalyst for catalytically activating MPS to eliminate HBA in water.

3.3. Effects of various PCNB and MPS dosages

As PCNB coupled with MPS could efficiently degrade HBA in water, it would be necessary to figure out the optimal conditions of PCNB and MPS dosages for further investigations. Fig. 5(b) shows the effect of different PCNB dosages on HBA degradation. As discussed in the earlier section, there was no adsorption of HBA on PCNB surface. Nevertheless, when PCNB was introduced (i.e., 75 mg/L), 90% of HBA was remarkably reduced in 60 min. Once the dosage of PCNB was increased to 100 mg/L,

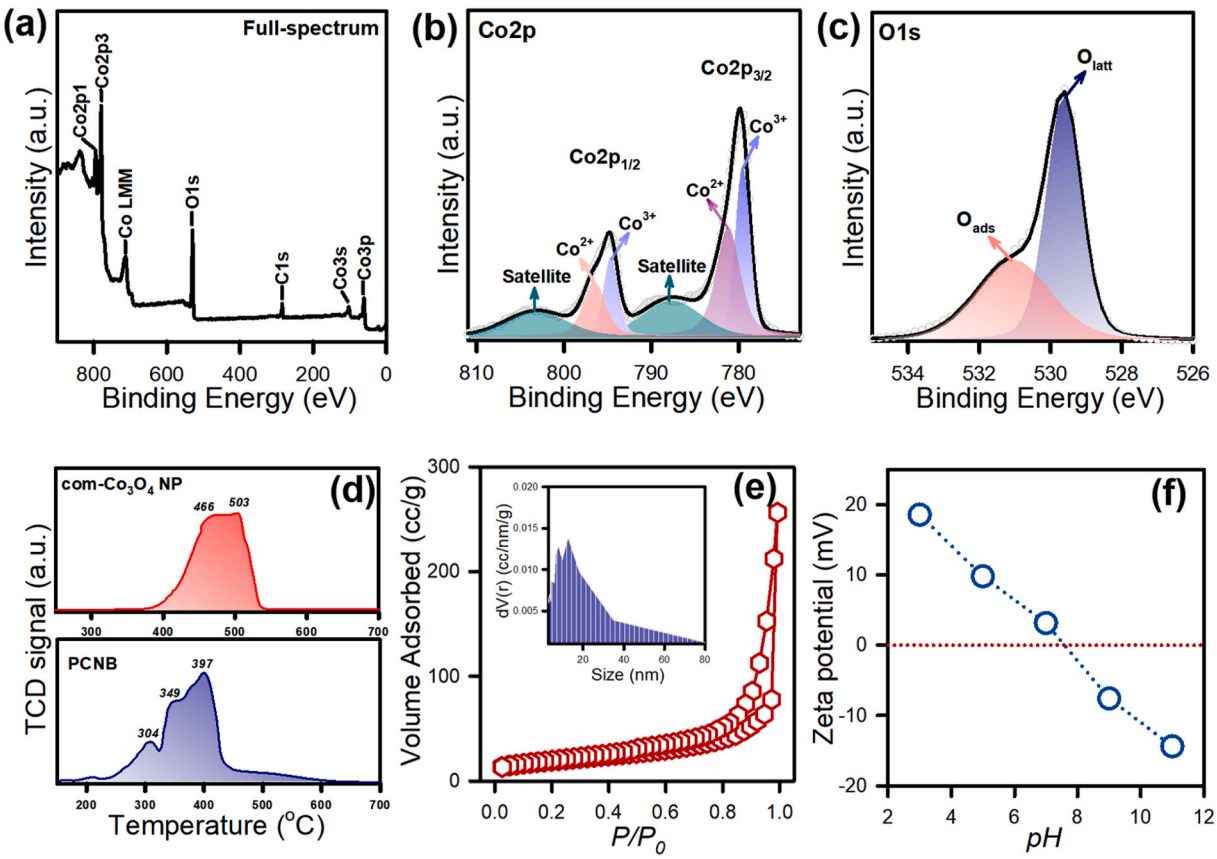

Fig. 4. XPS profiles of PCNB: (a) a full survey spectrum, (b) Co2p spectra, and (c) O1s spectra; (d) H_2-TPR profiles, (e) textural properties, and (f) zeta potentials of PCNB.

HBA was instantly and completely degraded within 30 min whereas the complete HBA degradation could be achieved in 20 min at a higher PCNB dosage of 150 mg/L. This result confirmed that the HBA degradation efficiency was improved at higher dosages of PCNB with more active sites contributing to enhance MPS activation. To further reveal the positive effect of higher PCNB dosages for activating MPS, the degradation kinetics of HBA at various PCNB dosages were further calculated using the pseudo 1st-order equation as following (Eq. (1)) (Wang et al., 2017b):

$$\ln(C_t/C_0) = -kt \quad (1)$$

where k value represents the reaction rate. The k values at different PCNB dosages were shown in the inset of Fig. 5(b). Specifically, the corresponding k values were determined as 0.07 min^{-1}, 0.117 min^{-1}, and 0.239 min^{-1} at PCNB dosage of 75 mg/L, 100 mg/L, and 150 mg/L, respectively. This result assured the enhancement of higher PCNB dosages for MPS activation to rapidly eliminate HBA.

On the other hand, since MPS plays a crucial role in the degradation of HBA, the effect of MPS dosages was also studied. Fig. 5(c) reveals that at MPS = 100 mg/L, HBA was not fully degraded as C_t/C_0 could only reach 0.2 in 60 min, implying that insufficient $SO_4^{\bullet-}$ radicals were generated to completely degrade HBA. Nonetheless, once MPS dosage increased to 150 mg/L and 200 mg/L, a full HBA degradation could be achieved as C_t/C_0 reached zero within 30 min and 20 min, respectively. This result indicated that the degradation efficiency of HBA was unfavorable at lower MPS dosage, possibly due to the insufficient production of $SO_4^{\bullet-}$ radicals whilst higher MPS dosages with sufficient generated $SO_4^{\bullet-}$ radicals were more advantageous. Besides, the corresponding k value (as displayed in the inset of Fig. 5(c)) was determined as 0.04 min^{-1} at 100 mg/L of MPS, which was noticeably raised to 0.117 min^{-1} at MPS = 150 mg/L and 0.148 min^{-1} at MPS = 200 mg/L, respectively, further validating the positive effect of higher MPS dosages on HBA degradation. Through these experimental results, it can be concluded that the degradation efficiency of HBA was certainly correlated with the concentrations of MPS while PCNB dosages would influence the HBA degradation kinetics. For further investigations, 100 mg/L of PCNB and 150 mg/L of MPS were particularly selected as optimal conditions to examine other parameters.

3.4. *Effects of temperatures, initial pH parameters, and co-existing compounds*

Since temperature represents an important parameter to HBA elimination, the effect of different temperatures was also studied. As illustrated in Fig. S5(a), the degradation efficiency of HBA was certainly noticeably enhanced when the temperatures increased from 30 to 50 °C. Particularly, at 30 °C, HBA was completely degraded within 30 min with its k = 0.117 min^{-1} (Fig. S6(a)). Once the temperature increased to 40 °C, the concentration of HBA was instantly reduced and reached to zero in 20 min, which was achieved in an even shorter time at 50 °C. The corresponding k values at 40 °C and 50 °C were also dramatically increased to 0.239 min^{-1} and 0.364 min^{-1}, respectively. This result validated the advantageous effect of higher temperatures on HBA degradation by PCNB-activated MPS. On the other hand, since the calculated k values increased along with the increase of temperatures, the correlation between k value and temperatures was further corresponded via the following Arrhenius equation (Eq. (2)):

$$\ln k = \ln A - E_a/RT \quad (2)$$

where R represents the universal gas constant, T is the solution temperature in Kelvin (K), A denotes as the pre-exponential factor, and E_a presents the activation energy of HBA degradation (kJ/mol). The

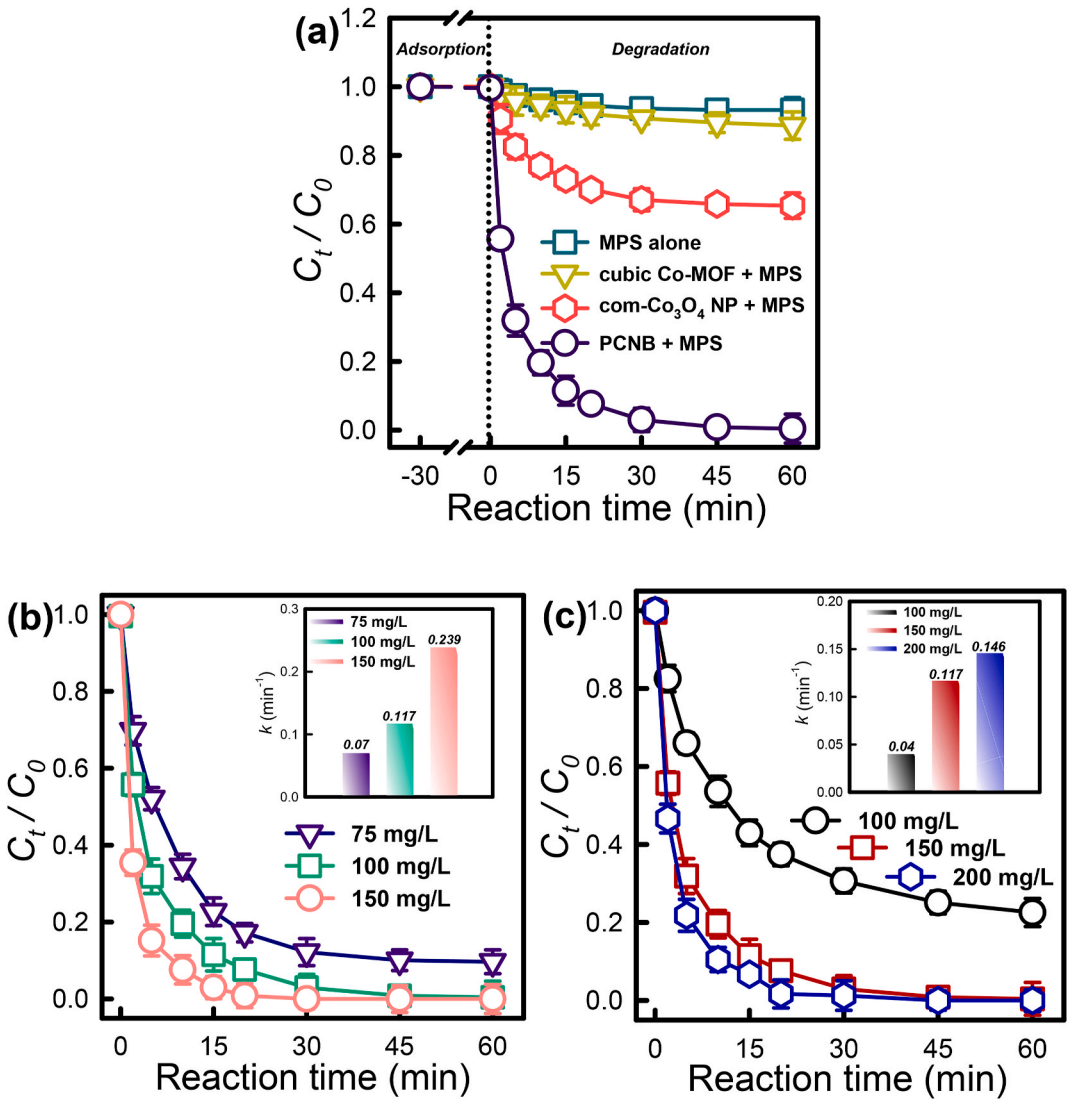

Fig. 5. (a) HBA degradation by different catalytic systems: MPS alone, pristine cubic Co-MOF + MPS, com-Co_3O_4 NP + MPS, and PCNB + MPS (catalyst = 100 mg/L, MPS = 150 mg/L, T = 30 °C). Effects of (b) PCNB dosage and (c) MPS dosage on HBA degradation (PCNB = 100 mg/L, MPS = 150 mg/L).

Arrhenius plot in the inset of Fig. S5(a) illustrates the relationship between ln k versus 1/T, which was then employed to determine the activation energy as 46.2 kJ/mol. For comparison, various E_a values calculated from different catalysts for MPS activation were summarized as shown in Table S1. The calculated E_a value using PCNB activated MPS was comparatively lower than other reported studies, indicating that PCNB was an efficient and competitive heterogeneous catalyst to activate MPS.

Additionally, as the initial pH parameters might also influence to the degradation efficiency of HBA using PCNB + MPS system, the effect of various initial pH values was further studied. Fig. S5(b) reveals that the degradation efficiency of HBA was certainly affected when the initial pH was changed. Specifically, at the original pH (i.e., 7), HBA was effectively and fully degraded in 30 min with $k = 0.117$ min^{-1} (Fig. S6(b)). Once the initial pH value was adjusted to pH = 5, a weak acidic condition, HBA degradation became slower as C_t/C_0 only reached 0.2 after 60 min as its k value was notably reduced to 0.045 min^{-1}. In the strongly acidic condition (i.e., pH = 3), the intense influence on HBA degradation could be noticed as C_t/C_0 was only 0.8 with $k = 0.006$ min^{-1}. This result revealed the adverse influence of acidic environment to HBA degradation using PCNB-activated MPS. This was possibly due to the high-stability of MPS at lower pH values (Tuan et al., 2021a; Tan et al., 2014). Besides, another reason should be related to the consumption of $SO_4^{\bullet-}$ and $^{\bullet}OH$ radicals by excessive H^+ ions as the following equations (Eq. (3) and (4)) (Lai et al., 2018), diminishing MPS activation capability, and thereby reducing the catalytic degradation efficiency.

$$H^+ + SO_4^{\bullet-} + e^- \rightarrow HSO_4^- \quad (3)$$

$$H^+ + {}^{\bullet}OH + e^- \rightarrow H_2O \quad (4)$$

$$SO_4^{\bullet-} + OH^- \rightarrow SO_4^{2-} + {}^{\bullet}OH \quad (5)$$

Moreover, the degradation efficiencies of HBA were also noticeably influenced at basic conditions. Particularly, when the initial pH was altered to the weak basic condition at pH = 9, HBA degradation effectiveness was comparatively decreased as C_t/C_0 only approached 0.4 after 60 min with $k = 0.026$ min^{-1}. When the initial pH was altered to strong basic condition at pH = 11, the degradation efficiency of HBA was drastically influenced as C_t/C_0 merely approached to 0.95 as its k value was only 0.001 min^{-1}. This result further indicated that HBA degradation was unfavorable under basic conditions, which probably due to the MPS activation with less generated $SO_4^{\bullet-}$ radicals at alkaline conditions since $SO_4^{\bullet-}$ radicals might be converted into $^{\bullet}OH$ radicals in the alkaline environment (Eq. (5)) which possessed lower redox potential and shorter life-span (<1 μs) (Rastogi et al., 2009), hence resulting in

deficient $SO_4^{\bullet-}$ radicals to HBA degradation. Furthermore, the presence of hydroxyl ions at basic environment might accumulate on the surface of PCNB, which made the surface charge of PCNB more negatively, then creating the electrostatic repulsion between the negative-charged surface of PCNB and $SO_5^{\bullet-}$, thereby diminishing the generation of $SO_4^{\bullet-}$ radical species (Guo et al., 2013).

On the other hand, as the natural water and actual wastewater are commonly comprised of other co-existing substances (e.g., inorganic salts, surfactants and natural organic matter (NOM)), which might affect to the degradation of HBA using PCNB + MPS; therefore, the effect of these co-existing species on HBA degradation was also examined as displayed in Fig. S5(c). First, the effect of NaCl, a typical salt, was evaluated at different concentrations. While HBA was still efficiently degraded in the presence of 500 mg/L of NaCl with $k = 0.076$ min^{-1} (Fig. S6(c)), the degradation efficiency of HBA was slightly influenced at a high concentration of NaCl (i.e., 5000 mg/L) as C_t/C_0 reached 0.1 after 60 min whereas its k was 0.053 min^{-1}. Since $SO_4^{\bullet-}$ might be consumed by Cl^- ions released from NaCl in the solution to form other chloride species (Wang et al., 2018; Ghanbari and Moradi, 2017), these as-formed chloride species have lower standard oxidation potentials than that of $SO_4^{\bullet-}$ radical species, thus restraining HBA degradation effectiveness. Nevertheless, more than 90% of HBA concentration was still degraded by PCNB-activated MPS, even at high-concentrations of NaCl which were obviously much higher than the initial concentration of HBA (i.e., 10 mg/L), revealing the highly-durable catalytic activity of PCNB to active MPS for HBA degradation.

$$HSO_5^- + Cl^- \rightarrow SO_4^{2-} + HOCl \quad (6)$$

$$2Cl^- + HSO_5^- + H^+ \rightarrow SO_4^{2-} + Cl_2 + H_2O \quad (7)$$

$$SO_4^{\bullet-} + Cl^- \rightarrow SO_4^{2-} + Cl^{\bullet} \quad (8)$$

$$Cl^{\bullet} + Cl^- \rightarrow Cl_2^{\bullet-} \quad (9)$$

In addition to Cl^-, various inorganic anions (i.e., bicarbonate (HCO_3^-), sulfate (SO_4^{2-})) were also employed to verify their influence to HBA degradation. As shown in Fig. S5(d), the degradation efficiency of HBA was negligibly influenced in the presence of co-existing SO_4^{2-} since almost 100% of HBA was degraded, and its k value was calculated as 0.073 min^{-1} (Fig. S6(d)). This result is correlated with reported literature when the redox potential of $SO_4^{\bullet-}/SO_4^{2-}$ reduced (Deng et al., 2018); however, SO_4^{2-} may also react with $^{\bullet}OH$ radicals to produce more $SO_4^{\bullet-}$ radicals (Eq. (10)) (Chen et al., 2021). On the other hand, it is reported that HCO_3^- may also react with free radicals to produce less powerful radicals (Eq. (11-12)), thus reducing the degradation efficiency (Qi et al., 2014). Therefore, it would be also necessary to examine the effect of bicarbonate to HBA degradation using PCNB-activated MPS. It can be noticed from Fig. S5(d) that HBA degradation was certainly influenced when HCO_3^- was introduced as C_t/C_0 approached 0.1 in 60 min, showing the inhibitory effect of HCO_3^- to HBA degradation, which was more pronounced in comparison with Cl^- and SO_4^{2-}. And its corresponding k value was also decreased to 0.043 min^{-1} (Fig. S6(d)). Moreover, as natural organic matter (NOM) is frequently detected in natural water, the presence of NOM may also influence the degradation of HBA by PCNB-activated MPS (Bai et al., 2020). Particularly, humic acid (HA), one of the main components of NOM, was selected in this study to verify the effect of NOM as depicted in Fig. S5(d). The degradation effectiveness of HBA was influenced when HA was introduced. Specifically, at HA = 5 mg/L, only 85% of HBA was degraded in 60 min, which was further decreased to 60% at a higher HA concentration (i.e., 10 mg/L). The corresponding degradation kinetics (k values) in the presence of different HA concentrations were also measured as 0.033 min^{-1} and 0.015 min^{-1} at 5 mg/L and 10 mg/L of HA, respectively (Fig. S6(d)). These results validated the negative influence of HA on HBA degradation, which possibly due to the competing interaction of HA and HBA during reaction. Pang and his co-colleagues found that HA could cause both positive and negative effects on MPS activation to degrade methylene blue, depending on the experimental conditions (Pang et al., 2018). The positive effect of HA on MPS activation could be attributed to its functional groups which are beneficial for activating MPS whereas the negative effect comes from the competing interaction between HA and target pollutant (Pang et al., 2018).

$$SO_4^{2-} + {}^{\bullet}OH \rightarrow SO_4^{\bullet-} + OH^- \quad (10)$$

$$SO_4^{2-} + HCO_3^- \rightarrow {}^{\bullet}HCO_3 + SO_4^{2-} \quad (11)$$

$$^{\bullet}OH + HCO_3^- \rightarrow {}^{\bullet}CO_3^- + H_2O \quad (12)$$

Besides, the presence of surfactants in water may also influence to the degradation efficiency of HBA using PCNB + MPS system. In this study, two particular surfactants, namely CTAB and SDS, were selected to examine the influence of co-existing surfactants on HBA degradation. As depicted in Fig. S5(c), in the presence of CTAB (500 mg/L), the degradation of HBA became slower as C_t/C_0 could only approach 0.3 and its k was 0.035 min^{-1} (Fig. S6(c)), implying the negative effect of CTAB to HBA degradation by PCNB + MPS system. As CTAB represents a cationic surfactant, the introduction of positively-charged CTAB into the HBA degradation might cause electrostatic attraction to both HBA and HSO_5^- (Li et al., 2020), which diminishes the approach of HBA and HSO_5^- to PCNB, leading to the lower degradation efficiency.

On the other hand, in the presence of 500 mg/L of SDS, the inhibitory effect of SDS on HBA degradation was even more pronounced as only *ca.* of 40% HBA was eliminated and the k was only 0.014 min^{-1}, revealing that the degradation of HBA using PCNB + MPS was unfavorable when SDS co-existed. Since SDS represents a typical anionic surfactant, the negatively-charged SDS might reside on the surface of PCNB, causing the electrostatic revulsion between HBA and PCNB (Tuan et al., 2020a), which possibly restricts the approach of HBA to PCNB, then decreasing the degradation effectiveness.

3.5. Mechanism for PCNB-activated MPS for HBA degradation

Since PNCB consisted of Co_3O_4 NPs, the cobaltic species in PCNB (i.e., Co^{3+} and Co^{2+}) would react with MPS to primarily produce $SO_4^{\bullet-}$ radical species which might then react with H_2O to generate $^{\bullet}OH$ radical species as following equations (Eq. (13-15)) (Xu et al., 2015, 2020; Abdul Nasir Khan et al., 2019):

$$Co^{2+}@PCNB + HSO_5^- \rightarrow Co^{3+}@PCNB + SO_4^{\bullet-} + OH^- \quad (13)$$

$$Co^{3+}@PCNB + HSO_5^- \rightarrow Co^{2+}@PCNB + SO_5^{\bullet-} + OH^- \quad (14)$$

$$SO_4^{\bullet-} + H_2O \rightarrow SO_4^{2-} + {}^{\bullet}OH + H^+ \quad (15)$$

As radical species might be derived from MPS activation, ESR analysis was typically employed to determine the existence of these species using DMPO as a radical spin-trapping agent. Fig. 6(a) reveals that there was no obvious pattern obtained in the presence of MPS and DMPO; however, when PCNB and MPS were introduced to DMPO, noticeable signals were observed, which could be assigned to the hyperfine splitting of DMPO-OH and DMPO-SO_4 adducts (Tuan et al., 2020c; Khan et al., 2018; Ding et al., 2019). This result validates that both $SO_4^{\bullet-}$ and $^{\bullet}OH$ radical species co-existed in the PCNB + MPS system, which caused the degradation of HBA.

In order to distinguish the contribution of these radical species to HBA degradation, the quenching experiment using two common radical scavengers, namely *t*-butanol (TBA) and methyl alcohol (MeOH), was conducted as shown in Fig. 6(b). The concentration of radical scavengers selected in this study was referred to reported literature (Trang et al., 2021; Tuan et al., 2020d; Nguyen et al., 2021). It can be noted that in the absence of α-H, TBA could react quickly with $^{\bullet}OH$ so TBA is commonly used to probe the existence of $^{\bullet}OH$ (Tuan et al., 2021a); while MeOH contains α-H, MeOH could scavenge both $^{\bullet}OH$ and $SO_4^{\bullet-}$ (Huang et al., 2014). As illustrated in Fig. 6(b), HBA degradation efficiency was

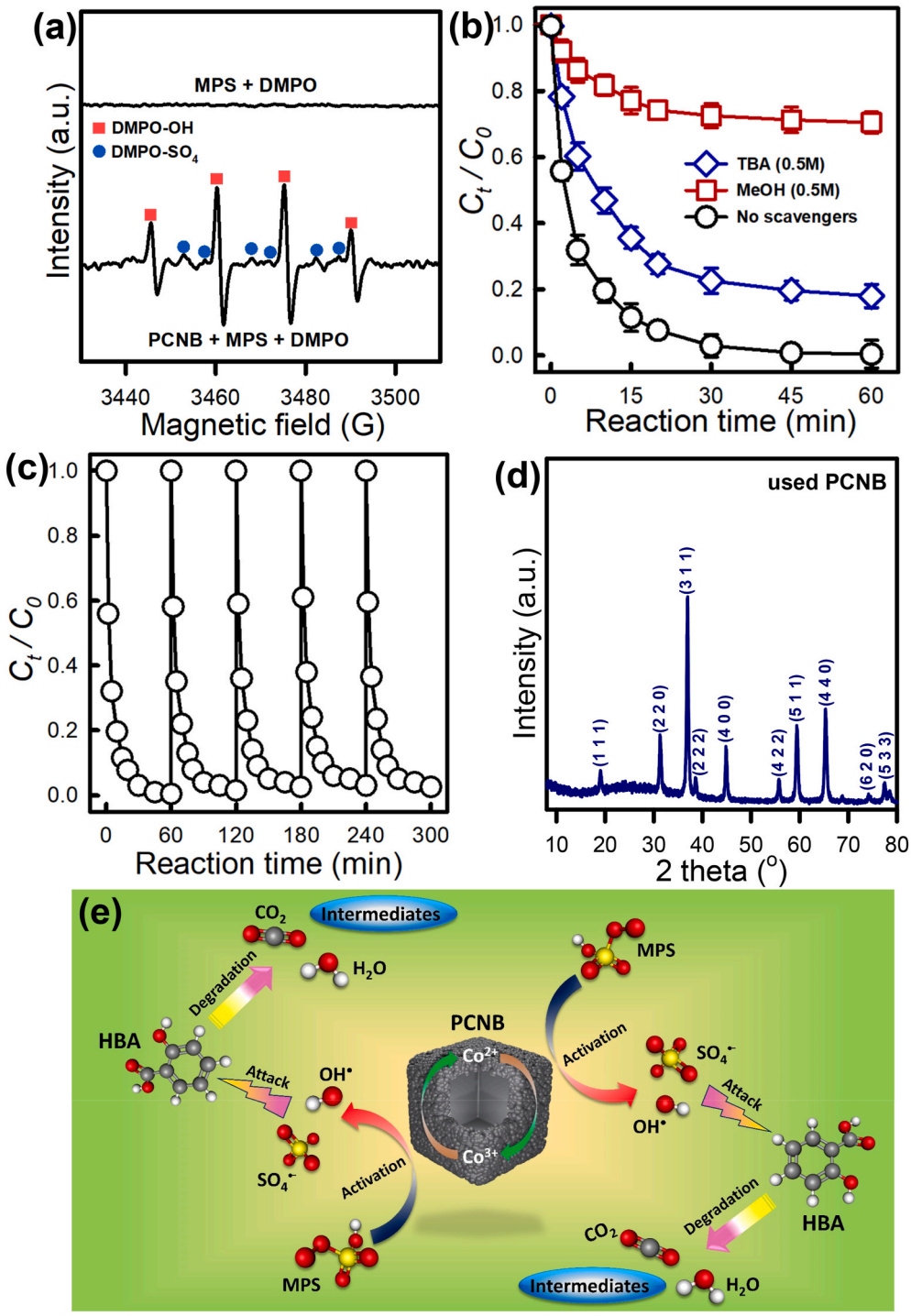

Fig. 6. (a) ESR analysis, (b) effect of radical scavengers on HBA degradation by PCNB + MPS; (c) reusability of PCNB over 5 consecutive HBA degradation cycles, and (d) XRD pattern of used PCNB (PCNB = 100 mg/L, MPS = 150 mg/L, T = 30 °C); (e) illustration of mechanism of HBA degradation by PCNB-activated MPS.

slightly inhibited in the presence of TBA as C_t/C_0 could reach 0.2 with its corresponding k was measured as 0.05 min^{-1} (Fig. S6(e)), suggesting the presence of •OH generated from PCNB + MPS, possibly contributing to the degradation of HBA. Besides, the degradation efficiency of HBA was critically inhibited when MeOH was introduced as C_t/C_0 merely approached 0.7 and the calculated corresponding k was only 0.011 min^{-1}. In order to further confirm the presence of •OH and SO_4•$^-$ radicals produced from MPS activation, different concentrations of MeOH and TBA were further employed. As illustrated in Fig. S7, the degradation efficiency of HBA in the presence of TBA (1 M) was almost similar with that of 0.5 M of TBA, indicating that 0.5 M of TBA was sufficient to quench all produced •OH radicals. Besides, the degradation of HBA was even further inhibited in the presence of MeOH (1 M) as C_t/C_0 merely approached 0.92 in 60 min. In addition to SO_4•$^-$ and •OH radicals, singlet oxygen ($^1O_2$) could be also produced from MPS activation, it would be also useful to verify the existence of $^1O_2$ derived from PCNB-activated MPS system. Typically, a quenching agent, namely sodium azide (NaN_3), was particularly selected for quenching test of $^1O_2$. As shown in Fig. S8(a), 100% of HBA degradation was still effectively afforded in the presence of NaN_3, suggesting that there was almost no

$^1O_2$ produced from PCNB + MPS system. Moreover, ESR analysis was further employed to examine the existence of $^1O_2$ using TEMP as a radical spin-trapping agent (Fig. S8(b)), and it would be easily noticeable that there was a very weak triplet signal detected from TEMP + MPS + PCNB system. This further proved that $^1O_2$ was barely produced from MPS activation and contributed to the degradation of HBA. This result illustrated that $SO_4^{\bullet-}$ and $^{\bullet}OH$ radical species were generated from PCNB + MPS system to involve in the degradation of HBA (as depicted in Fig. 6(e)), and $SO_4^{\bullet-}$ is the dominant species contributing to the degradation of HBA.

3.6. Reusability of PCNB for activating MPS to degrade HBA

Since HBA was effectively degraded using PCNB + MPS system, it was important to examine whether PCNB could be reusable to continuously activate MPS for consecutively various HBA degradation cycles. As shown in Fig. 6(c), the degradation effectiveness of HBA was remained comparatively over 5 consecutive cycles, in which more than 98% of HBA degradation was still achieved, indicating that PCNB could be highly reusable and its outstanding catalytic activity was certainly remained. On the other hand, the used PCNB exhibited comparable XRD patterns to PCNB before reactions without any significant changes as

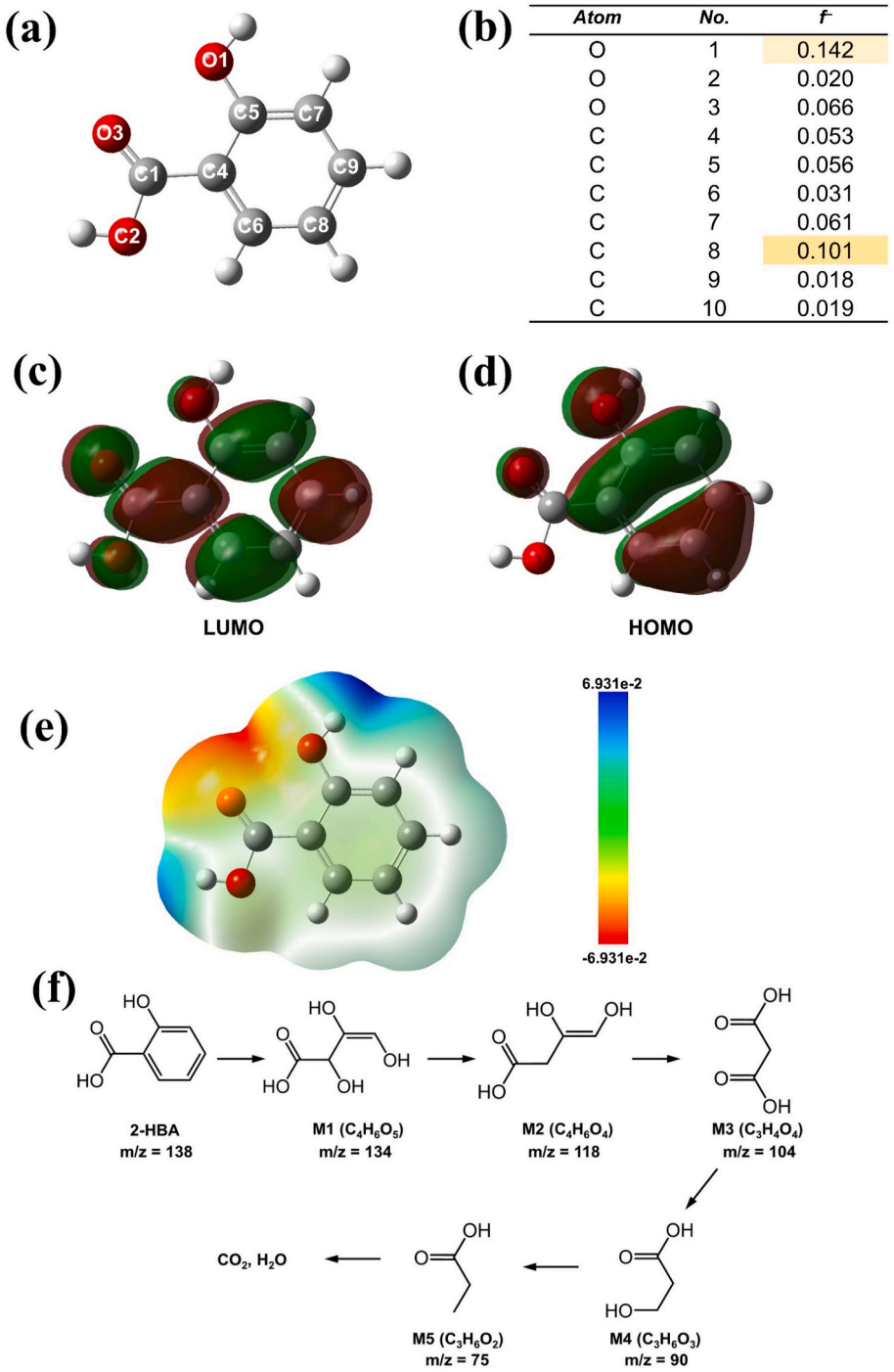

Atom	No.	f⁻
O	1	0.142
O	2	0.020
O	3	0.066
C	4	0.053
C	5	0.056
C	6	0.031
C	7	0.061
C	8	0.101
C	9	0.018
C	10	0.019

Fig. 7. Theoretical analysis for HBA: (a) LUMO, (b) HOMO of HBA; (c) Geometrically-Optimized HBA molecule; (d) Fukui index distributions; (e) Electrostatic potential-mapped molecular surface of HBA; and (f) a proposed degradation pathway of HBA.

displayed in Fig. 6(d). Furthermore, the Co2p core-level spectrum of the used PCNB was further analyzed. Fig. S9 shows that the positions of Co species in the used PCNB were retained in comparison with the pristine PCNB, proving the stability of PCNB; however, the proportion of Co^{2+}/Co^{3+} was changed, indicating the electron transfer between Co^{2+} and Co^{3+} during the oxidation reaction. This further the superior reusability and stability of PCNB, enabling it an efficient and robust heterogeneous catalyst to activate MPS for eliminating HBA from water. Besides, the Co leaching experiment was also examined in this study. Based on ICP analysis, the Co concentration over 5 degradation cycles was merely 0.08 mg/L, which is significantly smaller than the initial concentration of PCNB used in the experiment (i.e., 100 mg/L), illustrating that Co was negligibly leached out in the solution during the experimental processes. In order to verify the contribution of Co ions leached to MPS activation, homogeneous Co ions with the concentration of 0.08 mg/L were then used to activate MPS to degrade HBA as depicted in Fig. S10. One can be noticed that the concentration of HBA was merely changed in 60 min, illustrating that the degradation of BHA was mainly attributed to the catalytic activity of heterogeneous phase of Cobalt in PCNB.

3.7. Theoretic calculation, and a possible degradation process for HBA

Since PCNB exhibited the significant high catalytic activity for activating MPS to degrade HBA, it would be valuable to further examine how HBA was degraded by PCNB-activated MPS. For probing into the degradation mechanism, theoretical analysis of HBA using the density functional theory (DFT) was adopted specially to determine possible sites of HBA for receiving attack. The parameters of DFT calculation could be then found in the supporting information for obtaining the geometry optimization of HBA, Fukui index, molecule orbitals (MO), and electrostatic potential mapping analysis.

Firstly, Fig. 7(a) shows the geometrically-optimized HBA with its lowest unoccupied molecular orbital (LUMO), and highest occupied molecular orbital (HOMO) as illustrated in Fig. 7(c), and (d), respectively. In particular, the translucent-greenish, and translucent-reddish regions represent electron-insufficient, and electron-abundant regions of HBA. These electron-abundant regions would be prone to denoting electrons, and therefore, these regions would draw attacks from electrophilic ROS, namely, $SO_4^{\bullet -}$, and •OH. Fig. 7(b) also lists Fukui indices (i.e., f^-) of each site in HBA, and a site with the highest Fukui index (f^-)) would attract electrophilic (i.e., radical) attacks. Among all sites, the O1 site actually showed the highest f^- value, followed by the C8 site. Since the O1 site was a saturated site, and thus the C8 site appeared as the most possible site to draw attacks. Consequently, HBA might be attacked and oxidized starting from the C8 site in the benzene ring. In addition, the electrostatic potential (ESP) of HBA (Fig. 7(d)) also indicates that the C8 site would be prone to drawing radicals, leading to the decomposition of HBA.

Moreover, the degradation pathway of HBA was further validated through identification of intermediates of degradation. In view of the observed intermediates detected by a mass spectrophotometer (Fig. S11), a possible degradation pathway of HBA was then proposed as shown in Fig. 7(f). Initially, the benzene ring of HBA was firstly attacked to undergo the ring-opening reaction, and then transform into *2,3,4-Trihydroxy-3-butenoic acid* (M1). Next, M1 would be further oxidized to eliminate the hydroxyl group on the side, becoming *3,4-Dihydroxy-3-butenoic acid* (M2). Then, M2 would be further attacked to become *malonic acid* (M3), which would be further decomposed to afford *3-hydroxypropanoic acid* (M4), and *propionic acid* (M5) later. Eventually, these small molecules would be decomposed to CO_2, and H_2O.

4. Conclusion

In this work, a special Co_3O_4-based material was successfully fabricated derived from a cobaltic metal organic framework (Co-MOF). Through a surfactant-assisted strategy, a cubic Co-MOF was first prepared and employed as a precursor, which was then modified via chemical-etching process with TAN to afford hollow structure, and subsequently transformed into hollow porous Co_3O_4 nanobox (PCNB) via calcination. Through characterizations, this PCNB exhibited distinct reactive surface with abundant surface oxygen vacancy as well as physical properties compared with that of com-Co_3O_4 NP, which contributed to the outstanding catalytic activity of PCNB for activating MPS to degrade HBA in water. Besides, the activation energy (E_a) of 46.2 kJ/mol was also calculated using PCNB + MPS system, which was much lower than most of recent reported studies for activating MPS. Moreover, PCNB could be reusable over 5 consecutive HBA degradation cycles. These features make PCNB an effective and robust heterogeneous catalyst for catalytic activation of MPS to degrade a typical pharmaceutical and personal care product, namely HBA, in water.

Author contribution

Duong Dinh Tuan: Data curation, Writing – original draft; Cong Khiem: Data curation, Writing – original draft; Eilhann Kwon: Data curation; Yiu Fai Tsang: Data curation, Visualization, Investigation; Sanya Sirivithayapakorn: Data curation, Visualization, Investigation; Grzegorz Lisak: Writing- Reviewing and Editing; Bui Xuan Thanh: Writing – original draft preparation, Hongta Yang: Data curation, Visualization Investigation; Kun-Yi Andrew Lin: Data curation, Writing – original draft

Declaration of competing interest

The authors declare that they have no known competing financial interests or personal relationships that could have appeared to influence the work reported in this paper.

Appendix A. Supplementary data

Supplementary data to this article can be found online at https://doi.org/10.1016/j.chemosphere.2021.133441.

References

Abdul Nasir Khan, M., et al., 2019. Metal-organic framework-derived hollow Co3O4/carbon as efficient catalyst for peroxymonosulfate activation. Chem. Eng. J. 363, 234–246.

Andrew Lin, K.-Y., Chen, B.-C., 2016. Efficient elimination of caffeine from water using Oxone activated by a magnetic and recyclable cobalt/carbon nanocomposite derived from ZIF-67. Dalton Trans. 45 (8), 3541–3551.

Bai, R., et al., 2020. Acceleration of peroxymonosulfate decomposition by a magnetic MoS2/CuFe2O4 heterogeneous catalyst for rapid degradation of fluoxetine. Chem. Eng. J. 397, 125501.

Boullard, O., H. Leblanc, and B. Besson, Salicylic acid, in Ullmann's Encyclopedia of Industrial Chemistry.

Carmona, E., Andreu, V., Picó, Y., 2014. Occurrence of acidic pharmaceuticals and personal care products in Turia River Basin: from waste to drinking water. Sci. Total Environ. 484, 53–63.

Chen, X., et al., 2021. Degradation of tetracycline hydrochloride by coupling of photocatalysis and peroxymonosulfate oxidation processes using CuO-BiVO4 heterogeneous catalyst. Process Saf. Environ. Protect. 145, 364–377.

de Rivas, B., et al., 2011. Synthesis, characterisation and catalytic performance of nanocrystalline Co3O4 for gas-phase chlorinated VOC abatement. J. Catal. 281 (1), 88–97.

Deng, J., et al., 2017. Heterogeneous activation of peroxymonosulfate using ordered mesoporous Co3O4 for the degradation of chloramphenicol at neutral pH. Chem. Eng. J. 308, 505–515.

Deng, J., et al., 2018. Magnetic MnFe2O4 activated peroxymonosulfate processes for degradation of bisphenol A: performance, mechanism and application feasibility. Appl. Surf. Sci. 459, 138–147.

Ding, M., et al., 2019. Heterogeneous Fe2CoTi3O10-MXene composite catalysts: synergistic effect of the ternary transition metals in the degradation of 2,4-dichlorophenoxyacetic acid based on peroxymonosulfate activation. Chem. Eng. J. 378, 122177.

Ebele, A.J., Abou-Elwafa Abdallah, M., Harrad, S., 2017. Pharmaceuticals and personal care products (PPCPs) in the freshwater aquatic environment. Emerging Contaminants 3 (1), 1–16.

Farhadi, S., Javanmard, M., Nadri, G., 2016. Characterization of Cobalt Oxide Nanoparticles Prepared by the Thermal Decomposition, 2016, vol. 63, p. 9, 2.

Fuchigami, T., et al., 2018. Complex three-dimensional Co3O4 nano-raspberry: highly stable and active low-temperature CO oxidation catalyst. Nanomaterials 8 (9), 662.
Ghanbari, F., Moradi, M., 2017. Application of peroxymonosulfate and its activation methods for degradation of environmental organic pollutants: Review. Chem. Eng. J. 310, 41–62.
Gong, D., Zeng, G.F., 2021. Low-temperature combustion of methane over graphene templated Co3O4 defective-nanoplates. Sci. Rep. 11 (1).
Guerra-Rodríguez, S., et al., 2018. Assessment of sulfate radical-based advanced oxidation processes for water and wastewater treatment: a review. Water 10 (12), 1828.
Guinea, E., et al., 2008. Mineralization of salicylic acid in acidic aqueous medium by electrochemical advanced oxidation processes using platinum and boron-doped diamond as anode and cathodically generated hydrogen peroxide. Water Res. 42 (1), 499–511.
Guo, W., et al., 2013. Degradation of antibiotics amoxicillin by Co3O4-catalyzed peroxymonosulfate system. Environ. Prog. Sustain. Energy 32 (2), 193–197.
Herrero, M., et al., 2007. Nanosize cobalt oxide-containing catalysts obtained through microwave-assisted methods. Catal. Today 128 (3), 129–137.
Hu, P., Long, M., 2016. Cobalt-catalyzed sulfate radical-based advanced oxidation: a review on heterogeneous catalysts and applications. Appl. Catal. B Environ. 181, 103–117.
Hu, H., et al., 2015. In situ DRIFTs investigation of the low-temperature reaction mechanism over Mn-doped Co3O4 for the selective catalytic reduction of NOx with NH3. J. Phys. Chem. C 119 (40), 22924–22933.
Hu, R., Zhang, L., Hu, J., 2016. Study on the kinetics and transformation products of salicylic acid in water via ozonation. Chemosphere 153, 394–404.
Huang, Z., et al., 2014. Novel green activation processes and mechanism of peroxymonosulfate based on supported cobalt phthalocyanine catalyst. Appl. Catal. B Environ. 154–155, 36–43.
Karnik, B.S., et al., 2007. Use of salicylic acid as a model compound to investigate hydroxyl radical reaction in an ozonation–membrane filtration hybrid process. Environ. Eng. Sci. 24 (6), 852–860.
Khan, A., et al., 2018. Facile synthesis of yolk shell Mn2O3@Mn5O8 as an effective catalyst for peroxymonosulfate activation. Phys. Chem. Chem. Phys. 20 (20), 13909–13919.
Lai, L., et al., 2018. Co/Al2O3-EPM as peroxymonosulfate activator for sulfamethoxazole removal: performance, biotoxicity, degradation pathways and mechanism. Chem. Eng. J. 343, 676–688.
Lapworth, D.J., et al., 2018. Deep urban groundwater vulnerability in India revealed through the use of emerging organic contaminants and residence time tracers. Environ. Pollut. 240, 938–949.
Li, M.-C., et al., 2020. Enhanced degradation of 5-sulfosalicylic acid using peroxymonosulfate activated by ordered porous silica-confined Co3O4 prepared via a solvent-free confined space strategy. Separ. Purif. Technol. 249, 116972.
Lin, K.-Y.A., Chang, H.-A., 2015. Ultra-high adsorption capacity of zeolitic imidazole framework-67 (ZIF-67) for removal of malachite green from water. Chemosphere 139, 624–631.
Liu, Y., et al., 2019. Activation of persulfate with metal–organic framework-derived nitrogen-doped porous Co@C nanoboxes for highly efficient p-Chloroaniline removal. Chem. Eng. J. 358, 408–418.
Liu, Y., et al., 2020. MOF-derived metal-free N-doped porous carbon mediated peroxydisulfate activation via radical and non-radical pathways: role of graphitic N and CO. Chem. Eng. J. 380, 122584.
Liu, Y., et al., 2021. Enhanced peroxydisulfate oxidation via Cu(III) species with a Cu-MOF-derived Cu nanoparticle and 3D graphene network. J. Hazard Mater. 403, 123691.
Nguyen, H.T., et al., 2021. Bamboo-like N-doped carbon nanotube–confined cobalt as an efficient and robust catalyst for activating monopersulfate to degrade bisphenol A. Chemosphere 279, 130569.
Otero, M., Grande, C.A., Rodrigues, A.E., 2004. Adsorption of salicylic acid onto polymeric adsorbents and activated charcoal. React. Funct. Polym. 60, 203–213.
Pang, Y., et al., 2018. Effect of humic acid on the degradation of methylene blue by peroxymonosulfate. Open Chemistry 16 (1), 401–406.
Qi, F., Chu, W., Xu, B., 2014. Modeling the heterogeneous peroxymonosulfate/Co-MCM41 process for the degradation of caffeine and the study of influence of cobalt sources. Chem. Eng. J. 235, 10–18.
Rastogi, A., Al-Abed, S.R., Dionysiou, D.D., 2009. Sulfate radical-based ferrous–peroxymonosulfate oxidative system for PCBs degradation in aqueous and sediment systems. Appl. Catal. B Environ. 85 (3), 171–179.
Savun-Hekimoglu, B., Ince, N.H., 2017. Decomposition of PPCPs by ultrasound-assisted advanced Fenton reaction: a case study with salicylic acid. Ultrason. Sonochem. 39, 243–249.
Silva, P.H., Oliveira, H.S., Batista, M.S., 2020. Redox effects in Cu, Co or Fe in oxides nanocrystals with high catalytic activity for the acetonitrile combustion. SN Appl. Sci. 2 (4), 649.
Tan, C., et al., 2014. Radical induced degradation of acetaminophen with Fe3O4 magnetic nanoparticles as heterogeneous activator of peroxymonosulfate. J. Hazard Mater. 276, 452–460.
Tang, C.-W., Wang, C.-B., Chien, S.-H., 2008. Characterization of cobalt oxides studied by FT-IR, Raman, TPR and TG-MS. Thermochim. Acta 473 (1), 68–73.
Trang, N.H., et al., 2021. Cobalt ferrite nanoparticle-loaded nitrogen-doped carbon sponge as a magnetic 3D heterogeneous catalyst for monopersulfate-based oxidation of salicylic acid. Chemosphere 267, 128906.
Tsai, Y.-C., et al., 2020. Catalytic soot oxidation using hierarchical cobalt oxide microspheres with various nanostructures: insights into relationships of morphology, property and reactivity. Chem. Eng. J. 395, 124939.
Tuan, D.D., Lin, K.-Y.A., 2018. ZIF-67-derived Co3O4 rhombic dodecahedron as an efficient non-noble-metal catalyst for hydrogen generation from borohydride hydrolysis. J. Taiwan Inst. Chem. Eng. 91, 274–280.
Tuan, D.D., et al., 2020a. Porous hexagonal nanoplate cobalt oxide derived from a coordination polymer as an effective catalyst for activating Oxone in water. Chemosphere 261, 127552.
Tuan, D.D., et al., 2020b. Cobalt-based coordination polymer-derived hexagonal porous cobalt oxide nanoplate as an enhanced catalyst for hydrogen generation from hydrolysis of borohydride. Int. J. Hydrogen Energy 45 (56), 31952–31962.
Tuan, D.D., et al., 2020c. Coordination polymer-derived cobalt-embedded and N/S-doped carbon nanosheet with a hexagonal core-shell nanostructure as an efficient catalyst for activation of oxone in water. J. Colloid Interface Sci. 579, 109–118.
Tuan, D.D., et al., 2020d. Coordination polymer-derived porous Co3O4 nanosheet as an effective catalyst for activating peroxymonosulfate to degrade sulfosalicylic acid. Appl. Surf. Sci. 532, 147382.
Tuan, D.D., et al., 2021a. Covalent organic polymer derived carbon nanocapsule–supported cobalt as a catalyst for activating monopersulfate to degrade salicylic acid. J. Environ. Chem. Eng. 9 (4), 105377.
Tuan, D.D., et al., 2021b. Enhanced reduction of bromate in water by 2-dimensional porous Co3O4 via catalytic hydrogenation. J. Environ. Chem. Eng. 9 (5), 105809.
Wang, Z., et al., 2016. Surface oxygen vacancies on Co3O4 mediated catalytic formaldehyde oxidation at room temperature. Catal. Sci. Technol. 6 (11), 3845–3853.
Wang, Y., et al., 2017a. Removal of pharmaceuticals and personal care products from wastewater using algae-based technologies: a review. Rev. Environ. Sci. Biotechnol. 16 (4), 717–735.
Wang, Q., et al., 2017b. Activation of peroxymonosulfate by Al2O3-based CoFe2O4 for the degradation of sulfachloropyridazine sodium: kinetics and mechanism. Separ. Purif. Technol. 189, 176–185.
Wang, N., et al., 2018. Prussian blue analogues derived porous nitrogen-doped carbon microspheres as high-performance metal-free peroxymonosulfate activators for non-radical-dominated degradation of organic pollutants. J. Mater. Chem. 6 (3), 884–895.
Wang, J., et al., 2021. Development of a novel 2D Ni-MOF derived NiO@C nanosheet arrays modified Ti/TiO2NTs/PbO2 electrode for efficient electrochemical degradation of salicylic acid wastewater. Separ. Purif. Technol. 263, 118368.
Wu, W.-C., Yang, C.-S., Chang, C.-C., 2019. Photo-degradation of salicylic acid over ruthenium oxide incorporated titania bifunctional photo-catalyst: an approach for direct cleavage of CaroO bond via hydro-deoxygenation. Molecular Catalysis 478, 110560.
Xu, L.J., Chu, W., Gan, L., 2015. Environmental application of graphene-based CoFe2O4 as an activator of peroxymonosulfate for the degradation of a plasticizer. Chem. Eng. J. 263, 435–443.
Xu, H., et al., 2020. Heterogeneous activation of peroxymonosulfate by a biochar-supported Co3O4 composite for efficient degradation of chloramphenicols. Environ. Pollut. 257, 113610.
Zhang, S.Y., et al., 2018. Co3O4 polyhedrons with enhanced electric conductivity as efficient water oxidation electrocatalysts in alkaline medium. J. Mater. Sci. 53 (6), 4323–4333.